Axial Compressive Behavior of Circular Stainless Steel Tube Confined UHPC Stub Columns under Monotonic and Cyclic Loading

Bing-Lin Lai [a,b,*], Yi-Ran Li [a], Jurgen Becque [c], Yu-Yang Zheng [a], Sheng-Gang Fan [a]

[a] Key Laboratory of Concrete and Prestressed Concrete Structures of Ministry of Education, School of Civil Engineering, Southeast University, Jiulonghu Campus, Nanjing 211189, China
[b] Key Lab of Structures Dynamic Behavior and Control of the Ministry of Education, Harbin Institute of Technology, Harbin, 150090, China
[c] Department of Engineering, University of Cambridge, Cambridge CB2 1PZ, UK

Abstract

A novel type of composite column consisting of an ultra-high performance concrete core confined by a stainless steel tube (SS+UHPC column) was investigated. The system is characterized by excellent corrosion resistance, aesthetic appearance, high axial capacity and pronounced ductility. An experimental programme comprising 14 SS+UHPC stub columns was carried out, covering both monotonic and cyclic loading. The main parameters varied in the experiments were the column diameter, the tube thickness and the loading scheme (monotonic or cyclic). The resulting load-displacement curves, failure modes, strain characteristics, axial capacities, confining pressures, stiffness degradation and ductility indices were thoroughly analyzed. The applicability of current empirical formulae in predicting the confined strength of UHPC in SS+UHPC columns was also examined, and found to be inadequate. Therefore, a new equation linking the confining pressure to the confined strength of UHPC was developed. Based on this, a design equation to quantify the axial capacity of SS+UHPC columns was presented.

Keywords: stainless steel; steel tube confined concrete (STCC) columns; ultra-high performance concrete (UHPC); axial performance; cyclic loading; monotonic loading

1. Introduction

Carbon steel structures and steel-concrete composite structures alike are prone to corrosion in aggressive environments, for instance in marine and offshore applications. This potentially compromises structural safety as well as durability, and increases maintenance and rehabilitation cost. Fig.1 shows a few examples of corrosion phenomena in steel offshore wind turbine structures, oil platforms and cross-sea bridges. When aiming to prolong the service life of offshore structures and improve their structural performance, stainless steel can offer a viable and sustainable alternative to carbon steel [1, 2].

(a) Wind turbine (b) Oil platform (c) Cross-sea bridge

Fig. 1 Typical corrosion phenomena of carbon steel structures in offshore engineering

In addition to its excellent corrosion resistance and aesthetic appearance, stainless steel also possesses pronounced strain hardening properties and outstanding ductility (particularly in the austenitic grades), making it an ideal material to be employed in concrete-filled steel tubular (CFST) columns, where the stainless steel tube offers a significant confinement effect to the infilled concrete by [3-15]. However, the high up-front cost limits the use of stainless steel alloys at large scale in structures. Stainless steel is therefore ideally used in thin-walled applications, which may then become prone to local buckling phenomena [16]. Previous research on concrete-filled tubular columns (e.g. [17-19]) has established that the confining steel tube could ideally be used as a 'jacket', such that yielding develops uniaxially in the circumferential (hoop) direction of the tube, to the full benefit of the confining effect, rather than the steel tube directly participating in carrying vertical load and yielding in a biaxial stress

state. The difference between the two states is illustrated in Fig. 2, where the latter state is referred to as a 'steel tube confined concrete' (STCC) column. To promote the development of the STCC stress state and avoid direct bearing stresses onto the steel, the steel tube may be terminated just short of the column ends (Fig. 2b). It is noted, however, that due to the presence of interfacial bond and friction between the steel tube and the concrete, the steel tube may inevitably still sustain some portion of the axial force over the course of loading [17]. Further to maximizing confinement to the concrete core, STCC columns also have the advantage that the steel tube is much less susceptible to local buckling, as axial compressive stresses in the steel tube have been minimized.

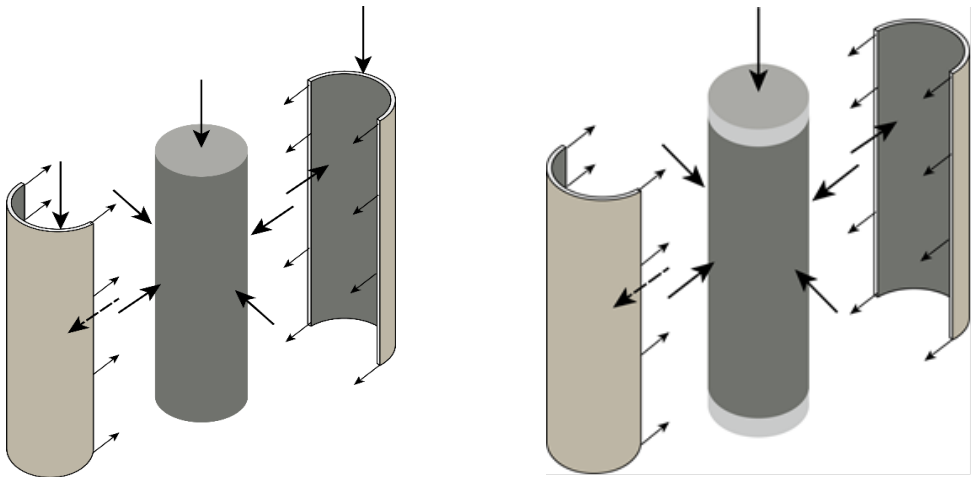

(a) Conventional CFST column (b) STCC column

Fig. 2 Comparison of load-carrying mechanisms of CFST column and STCC column

Comparative experimental investigations between STCC and CFST stub columns have previously been carried out, which demonstrated that the axial capacity of STCC stub columns is indeed higher than that of CFST stub columns due to the stronger confinement effect [24, 25]. Based on this test data, two sets of formulae were proposed to predict the axial capacity. A unified formulation, applicable to both STCC and CFST columns under axial compression, was presented by Li et al. [26], along with an analytical solution for the elastic deformation of circular STCC under specific boundary conditions. In other research [19, 27] compressive loading experiments were conducted on STCC columns with different cross-sectional shape,

featuring additional reinforcement within the core concrete, and the effects of the diameter/width-to-thickness ratios of the tubes, and bond and friction between tube and concrete on the failure modes and capacities were analysed. Corresponding formulae to predict their axial capacity were also presented. Liu et al. [28, 29] conducted experimental studies on STCC columns under both monotonic or cyclic compression, and investigated the failure modes, load-displacement curves, stress and strain states of the steel tube, and interaction behaviour between the steel tube and the concrete core, as a function of the design parameters. Le Hoang et al. [30, 31] conducted numerical research on STCC columns using the ATENA-3D software, taking the effect of concrete strength into account and proposing a simplified formula to predict the capacity.

While most of the previous research work in this area has focused on normal strength concrete columns confined by carbon steel tube, this research proposes a novel type of composite column, composed of Ultra High Performance Concrete (UHPC) confined by stainless steel (SS) tube, from here on labelled as (SS+UHPC) composite columns. The aim is to maximize the advantages offered by both materials. Indeed, past research conducted by the authors has demonstrated the inherent brittleness of UHPC in compression [20-23], which may potentially be overcome by the confinement offered by the stainless steel tube, capitalizing on the work hardening and ductility offered by the latter. To fill the currently existing research gap, an experimental program was initiated containing 14 SS+UHPC columns, subjected to either monotonic or cyclic compression. The failure modes, capacities and behaviour were thoroughly examined to provide new insights for the purpose of facilitating the further analysis and design of SS+UHPC columns in engineering practice.

2. Test specimens: geometry and materials

2.1 Specimen design and preparation

A total of 14 SS+UHPC column specimens were included in this experimental programme, among which seven specimens were tested under monotonic compression and their seven nominally identical counterparts were tested under cyclic compression. The test variables included the diameter-to-thickness ratio (D/t) of the stainless steel tube, the cross-sectional dimensions (T133 & T180) and the loading scheme. The test matrix is summarized in Table 1. Since the emphasis of the investigation was placed on the cross-sectional capacity of these novel sections, all specimens were designed as stub columns with a height-to-diameter ratio (H/D) of about 3.0, so as to eliminate both end effects and overall stability failure. The D/t ratios ranged from 21.61 to 58.70, resulting in steel content ratios α between 0.07 and 0.2. It is noted that the D/t ratios in this study are lower than those reported by Guo et al. [25] and Qiao et al. [32] for stainless steel tube confined normal-strength concrete columns, because UHPC typically requires stronger confinement to overcome its brittleness [33, 34]. For ease of identification, each specimen is labelled after its tube diameter, tube thickness and loading scheme. For example, "T133-6-b" refers to the specimens with a 133 mm tube diameter and a 6 mm tube thickness which was cyclically loaded.

Table 1 Specimen details of SS+UHPC columns

Specimen	H (mm)	D (mm)	t (mm)	D/t	H/D	α	f_{co} (MPa)	f_y (MPa)	ξ	$N_{u,t}$ (kN)	I_{10}	Failure mode
T133-3-a	400	129.16	3.02	42.77	3.10	0.09	106.65	272.53	0.26	2101	7.95	S
T133-3-b	400	129.20	3.04	42.50	3.10	0.09	106.65	272.53	0.26	1937	7.53	S
T133-4-a	400	130.46	3.93	33.20	3.07	0.14	106.65	264.25	0.33	2203	8.28	S
T133-4-b	400	130.56	3.98	32.80	3.06	0.14	106.65	264.25	0.33	2131	7.77	S
T133-6-a	400	132.24	6.12	21.61	3.02	0.21	106.65	288.37	0.58	2453	9.38	B
T133-6-b	400	132.16	6.08	21.74	3.03	0.21	106.65	288.37	0.58	2377	8.91	B
T180-3-a	550	179.06	3.06	58.52	3.07	0.07	106.65	272.53	0.18	3233	7.99	S
T180-3-b	550	179.04	3.05	58.70	3.07	0.07	106.65	272.53	0.18	2998	8.08	S
T180-4-a	550	180.64	3.95	45.73	3.04	0.11	106.65	264.25	0.23	3575	8.00	S
T180-4-b	550	180.72	3.99	45.29	3.04	0.11	106.65	264.25	0.23	3475	8.26	S
T180-6-a	550	184.84	6.07	30.45	2.98	0.16	106.65	288.37	0.39	4110	8.14	S
T180-6-b	550	184.82	6.06	30.50	2.98	0.16	106.65	288.37	0.39	4022	8.35	S
T180-8-a	550	180.12	8.14	22.13	3.05	0.21	106.65	267.63	0.52	4289	8.35	B
T180-8-b	550	180.04	8.10	22.23	3.05	0.21	106.65	267.63	0.52	4191	8.65	B

Note: ξ is the confinement factor calculated as: $A_s f_y / A_c f_{co}$; $N_{u,t}$ and I_{10} refer to the measured axial capacity and ductility index of the SS+UHPC columns. 'S' and 'B' indicate shear failure and bulging failure, respectively. α is the steel content ratio calculated as A_s/A_c.

Seamless austenitic ASTM 304 stainless steel tube was employed in this study, as suggested by Guo et al. [25]. As shown in Fig. 3, the stainless steel tube was isolated from the load at both ends by leaving out a 10 mm wide circumferential strip at a distance of 30 mm from the ends.

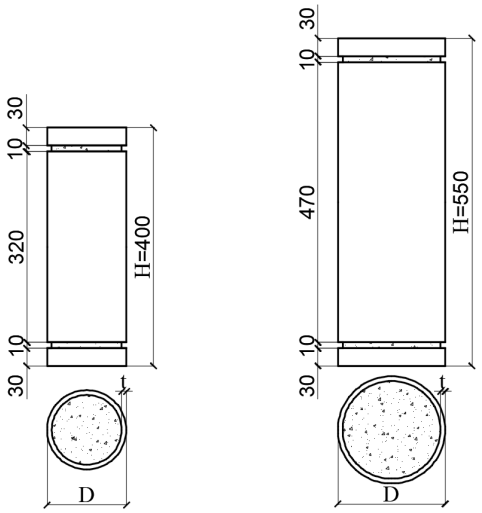

Fig. 3 SS+UHPC column geometry

All specimens were cast in one batch. Fig. 4 outlines the overall casting procedure of the SS+UHPC specimens. In a first step, the 30 mm wide end segments were aligned with the stainless steel tube and temporarily held in place by four longitudinal reinforcing bars, and the 10 mm gap was filled with polystyrene foam. After solidification of the polystyrene foam, the steel tube was placed on a tarp on level ground ready for UHPC casting. As pictured in Fig. 4 (c), a 2.0% volume fraction of copper coated steel fibers was added to the UHPC mix, purchased from Hunan Gu Li Engineering New Materials Co. Ltd. Although previous research suggests that steel fiber does not significantly affect the compressive behavior of CFST members [35, 36], it was nevertheless added to the mix, mainly for consistency with future planned studies on the flexural behaviour and axial-flexural interactive behaviour of SS+UHPC members. Fig. 4 (d) shows the completed specimens, where the polystyrene foam was removed from the gap. All specimens were cured under natural condition, together with the accompanying UHPC prism specimens and dog-bone specimens reserved for material tests.

Given that shrinkage of the UHPC may lead to an uneven surface, the top of the specimens was levelled and smoothed by applying a layer of mortar.

(a) End preparation (b) Tube before casting (c) UHPC mixing (d) Completed specimen

Fig. 4 SS+UHPC column manufacturing process

2.2 Material properties

The material properties of the stainless steel alloy were obtained from tensile coupon tests carried out in accordance with Chinese standard GB/T 228-2002 [37], while the properties of the UHPC were derived from compression tests in accordance with standard GB/T 50081-2002 [38]. The measured stress-stain curves are shown in Fig. 5, along with some images of the failed test specimens. It is seen that the austenitic 304 stainless steel exhibits pronounced nonlinearity in its stress-strain characteristics, as well as excellent ductility. As it does not display the yield plateau observed in typical carbon steel, the stress corresponding to 0.2% residual strain was employed to define the yield strength f_y, as per usual convention. As summarized in Table 1, the measured values of f_y were 272.53 MPa, 264.25 MPa, 288.37 MPa and 267.63 MPa for the tubes with thicknesses of 3 mm, 4 mm, 6 mm and 8 mm, respectively, and the corresponding elastic moduli were 218 GPa, 204 GPa, 227 GPa and 191 GPa [12]. The Poisson's ratio was measured to be 0.298 on average. The UHPC compressive prisms exhibited brittle failure without a descending stress-strain branch (Fig. 5b). The average compressive strength f_{co} was found to be 106.65 MPa, which is slightly lower than the expected value of

about 120 MPa due to using normal curing conditions. The concrete tensile strength f_t and Young's modulus E_c reached 13.1 MPa and 49.08 GPa, respectively, and the tensile stress-strain curve exhibited non-negligible post-peak resistance and ductility due to the fiber bridging effect (Fig. 5c) [39-41].

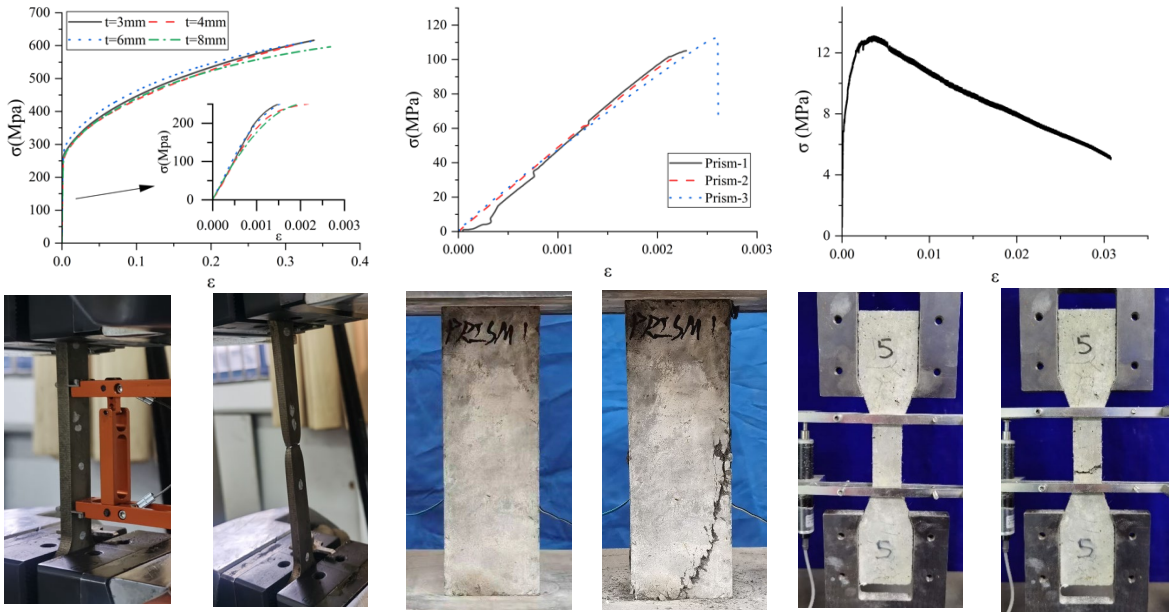

(a) Stainless steel tensile test (b) UHPC compression test (c) UHPC tensile test

Fig. 5 Material tests on stainless steel and UHPC

3. Experimental program

3.1 Test set-up and instrumentation

All tests were conducted in the Structural Laboratory of Southeast University using the 5000 kN high-stiffness compression machine. As shown in Fig. 6, the axial force was applied by moving the bottom platen of the testing machine, and four Linear Variable Differential Transformers (LVDTs) were installed at the corners of the platen to track the axial displacement of the SS+UHPC columns. Strain gauges were affixed at three locations along the height of specimens, a quarter-height apart (Fig. 6c). At the top and bottom location two horizontal stain gauges were attached to measure the lateral expansion of the stainless steel tube, while at mid-height horizontal and vertical strain gauges were attached at 120 degree intervals around the circumference.

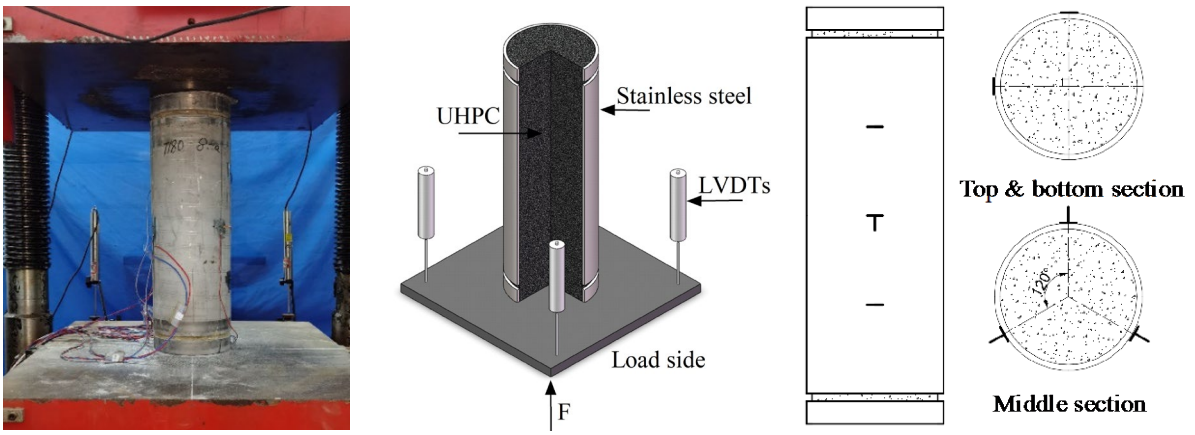

(a) Test setup (b) LVDT arrangement (c) Strain gauge arrangement

Fig. 6 Test set-up and instrumentation

A preloading stage up to 30% of the predicted maximum load was applied to the specimens to ensure the concentricity of the loading and the satisfactory functioning of all measuring devices. In the case of the monotonically loaded specimens, the loading was initially applied in a force-controlled manner at a rate of 3 kN/s. When the load reached 70% of the predicted axial capacity, the protocol was switched to a displacement-controlled scheme with a rate of 0.5 mm/min. This was increased to 1.0 mm/min after the specimens had entered the descending branch of the load-displacement curve and the residual capacity had stabilized. The test was terminated when the axial displacement reached 40 mm (for the T133 specimens) or 50 mm (for the T180 specimens), significant bulging, buckling, or shear deformation was observed, or a loud crushing sound was heard emanating from the UHPC. In the case of cyclic loading, the loading protocol proposed by Fang et al. [42] was employed, owing to the lack of a universally agreed scheme. Loading was initiated at a rate of 3 kN/s. Upon reaching 60% of the predicted static capacity, the specimen was unloaded at a rate of 6 kN/s. In order to always maintain contact between the specimen and the hydraulic machine, the unloading branch was terminated at a (relatively small) residual load of 100 kN, rather than at 0 kN. Subsequently, the specimen was loaded to 90% of the predicted maximum load, unloaded and reloaded. Past this stage displacement-controlled loading was employed and another five unloading/reloading cycles

were applied in the post-peak range with increasing displacement intervals of roughly 2 mm, 3 mm, 4 mm, 5 mm and 6 mm for the T133 specimens, and 2 mm, 4 mm, 6 mm, 8 mm and 10 mm for the T180 specimens. After completing these cycles, the specimen was further continually deformed at a rate of 1mm/min.

3.2 Test observations

Regardless of the loading scheme (monotonic or cyclic) the SS+UHPC composite columns were seen to fail in one of two possible modes: outward bulging failure ('barrelling') or shear failure. As shown in Fig. 7 (a), shear failure is characterized by failure along an oblique plane of maximum shear stress at an inclination of about 60-70 degrees with the horizontal plane. This failure mode typically occurs in specimens without sufficient confinement [43]. When removing the stainless steel tube from the specimens after the test, an almost complete separation of the UHPC core into two wedges was observed, indicating that the fiber-bridging effect could not effectively prevent the shear crack. The stainless steel tube also suffered localized plastic deformations at the end of the concrete shear plane. It is noteworthy that the UHPC was easily separated from the stainless steel tube after cutting the tube in two halves longitudinally, and no UHPC debris remained stuck to the tube in any of the specimens. This is consistent with the observations by Qiao at al. [32], implying a low bond strength between the UHPC and the stainless steel tube.

(a) Shear failure (b) Bulging failure

Fig. 7 Externally and internally observed failure of SS+UHPC column specimens

Bulging failure happened in specimens with a thicker steel tube. This failure mode is illustrated in Fig. 7 (b). After removing the tube, the UHPC core remained intact without visible major cracks, indicating that the confining pressure exerted by the thick stainless steel tube was effective in alleviating the brittleness of the UHPC and hence in changing the failure mode of the SS+UHPC columns. The failure modes of all specimens are presented in Fig. 8. It was observed that the specimens in this programme with a *D/t* ratio less than 22 generally failed in the bulging mode, while the specimens with a *D/t* ratio exceeding 22 suffered from shear failure, irrespective of the loading scheme. The failure modes are also listed in Table 1.

T133-3-a T133-4-a T180-3-a T180-4-a T180-6-a

T133-3-b T133-4-b T180-3-b T180-4-b T180-6-b

(a) Specimens with shear failure

T133-6-a T133-6-b T180-8-a T180-8-b

(b) Specimens with bulging failure

Fig. 8 Failure modes of all SS+UHPC column specimens

3.3 Deformation behaviour

3.3.1 Load-displacement response

Fig. 9 presents the full-range load-displacement curves of the monotonically loaded specimens, where the axial displacement is taken as the average value measured by the four LVDTs. It is seen that the ascending portion of the curves exhibit linear elastic behavior up to 80%-90% of the maximum load, which is a direct consequence of the linear performance of UHPC in compression (see Fig. 5 (b)). The short elastoplastic stage before the peak load is mainly attributed to the confinement of the concrete and the nonlinear strain-hardening properties of the stainless steel (see Fig. 5 (a)). Beyond the peak load, the specimens experienced an abrupt drop in the load, followed by a stage where the axial load stabilized or, for specimens with a thick steel tube, hardening behaviour was observed. Based on further study of Figs. 9 (a) & (b), it was concluded that the post-peak behavior is strongly linked to the failure mode. Specimens failing in the shear mode displayed a more significant drop in load, and a more limited residual capacity was observed of 72% to 81% of the peak load. On the other hand, in the specimens undergoing bulging failure, owing to the strong confinement effect, the residual capacity was more substantial and even remained comparable to the peak load despite significant axial deformations. Therefore, the bulging failure could be regarded as a ductile failure mode in the SS+UHPC columns. This interpretation is consistent with the ASTM E2126 rules [44], which define ductility based on the portion of the load-displacement curve up until a 20% post-peak drop in load.

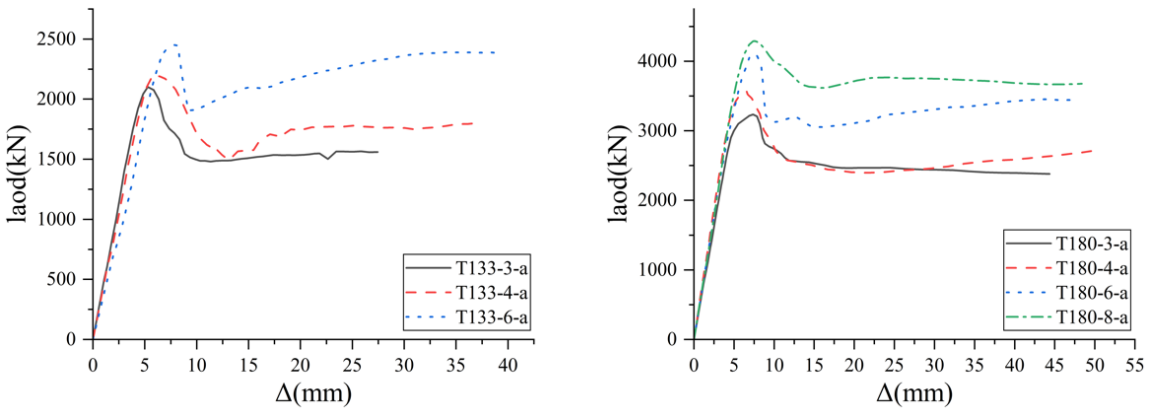

(a) T133 series (b) T180 series

Fig. 9 Axial load-displacement curves of monotonically loaded SS+UHPC columns

To evaluate the influence of the loading scheme, the load-displacement curves of the monotonically and cyclically loaded specimens are compared in Fig. 10. On a minor note, the first unloading cycle of the post-peak stage was accidentally mishandled in specimen T180-6-b, resulting in the larger than intended displacement gap in Fig. 10 (f). However, the prescribed protocol was still followed during subsequent cycles. With the possible exception of specimens T133-3-b and T133-4-b, the cyclic envelope curves coincide very well with their monotonic counterparts. Specimen T180-4-b even exhibits improved behaviour over the monotonic case in the fifth and sixth unloading/reloading cycles, which may be caused by the work hardening effect of the stainless steel under repeated loading cycles [45, 46]. As to the reasons why specimens T133-3-b and T133-4-b displayed a more notable strength decay after the peak load under cyclic loading (Fig. 10 (a) & (b)), these remain speculative and could be related to sub-par compaction of the UHPC, or fiber balling during the casting process. The effects of the resulting imperfections may be amplified by cyclic loading, with the accumulated damage resulting in a more sudden strength decay. These comments notwithstanding, it can be concluded that the cyclically loaded specimens exhibited a ductility and residual capacity comparable to their monotonic counterparts, indicating that the SS+UHPC columns are suitable for applications involving high-amplitude, low-cycle fatigue.

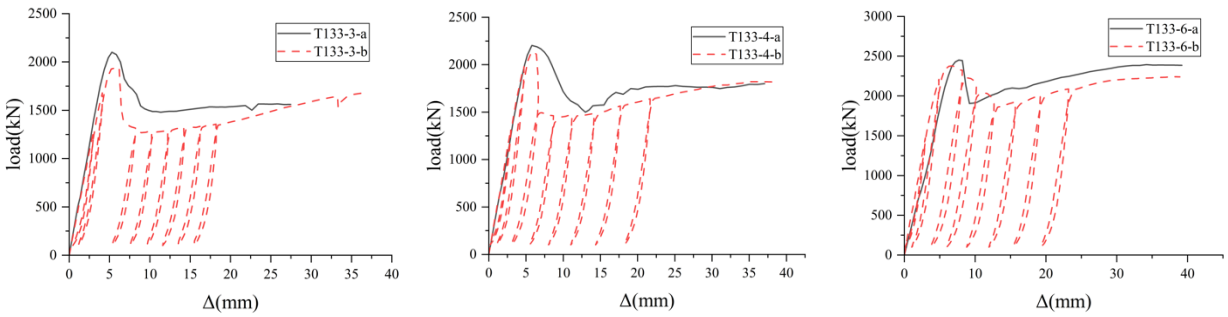

(a) T133-3-a/b (b) T133-4-a/b (c) T133-6-a/b

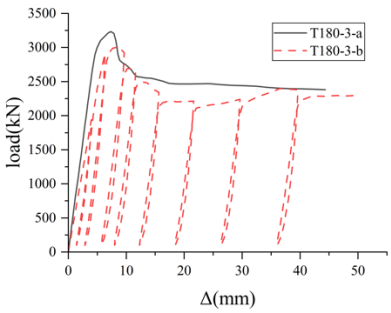

(d) T180-3-a/b

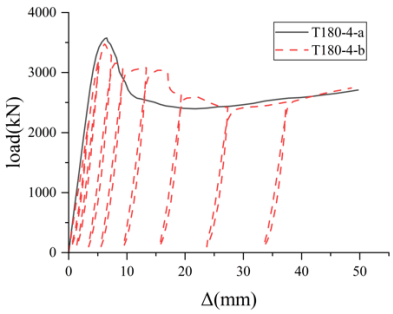

(e) T180-4-a/b

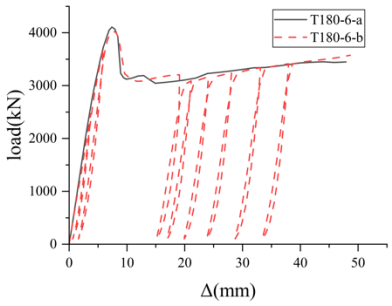

(f) T180-6-a/b

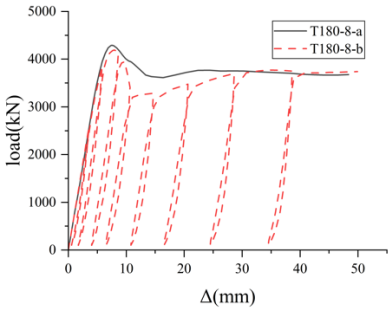

(g) T180-8-a/b

Fig. 10 Comparison of load-displacement curves between two loading schemes

3.3.2 Load-strain behaviour

To further explore the deformation response of the SS+UHPC columns, the load-strain curves obtained from the strain gauges on the stainless steel tube are plotted in Fig. 11. The graphs in Fig. 11 (a)-(g) show that the longitudinal strain in the tube is consistently larger than the hoop strain until the specimen reaches the peak load. This indicates that the steel tube carries significant axial force due to bond and friction in the steel-concrete interface, despite not being directly loaded. Before the peak load, consistent hoop strain readings were obtained at different section heights, which subsequently diverged in the post-peak range due to localized deformations in the tube.

Fig. 11 (h) presents the ($\varepsilon_h/\varepsilon_v$) ratio for the monotonically loaded SS+UHPC specimens over their loading history. It shows that $\varepsilon_h/\varepsilon_v$ increased from the onset of loading and exceeded the Poisson's ratio of stainless steel (about 0.3) in the early loading stage, indicating that some degree of confinement was activated even in the elastic range. This differs from conventional

CFST columns, where no appreciable confinement is generated until approaching the peak load, as a result of the Poisson's ratio of the steel exceeding that of the concrete (0.2). At the peak load, $\varepsilon_h/\varepsilon_v$ increased significantly, indicating the development of strong confinement.

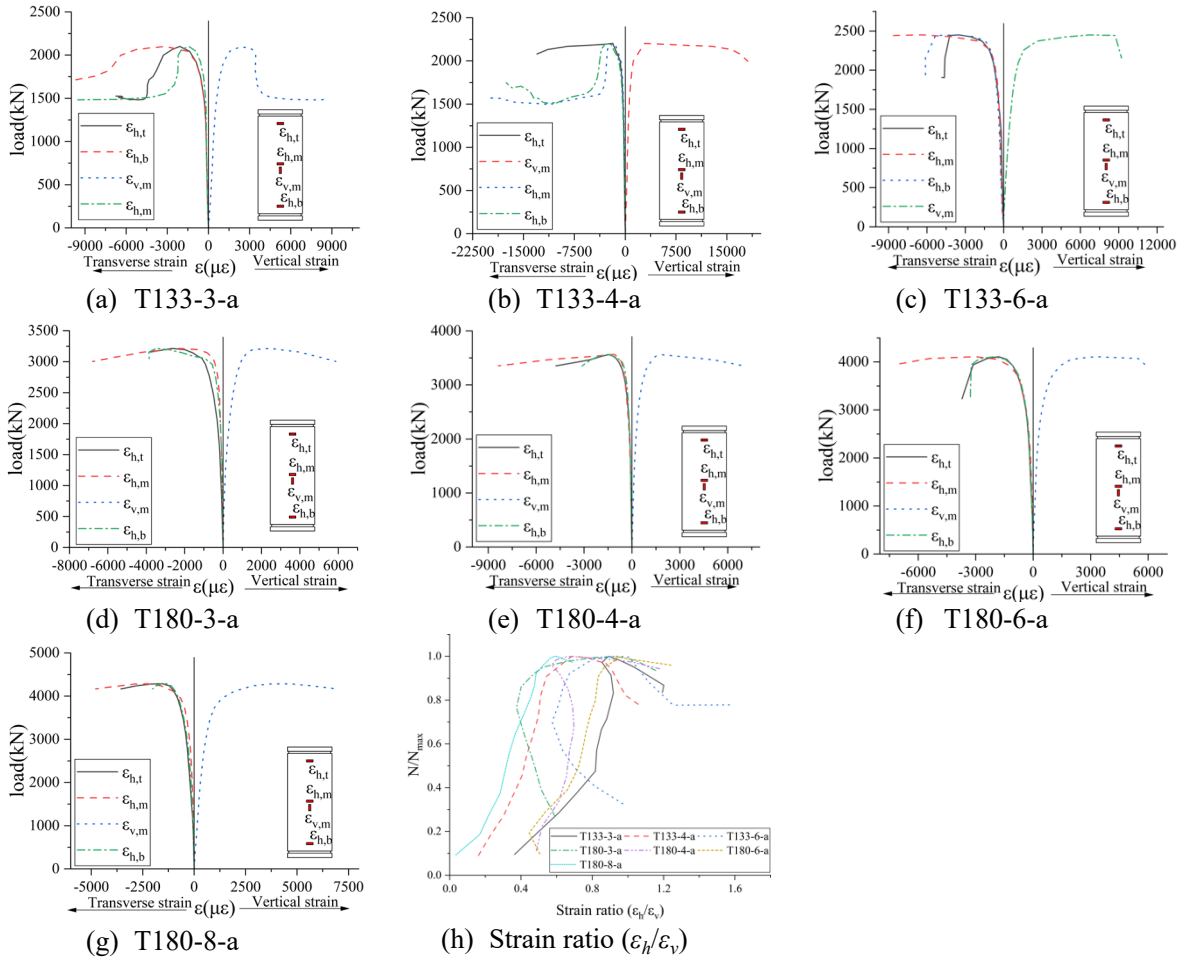

Fig. 11 Load-strain curves of monotonically loaded specimens

3.3.3 Stress analysis

The stainless steel tubes are sufficiently thin-walled to consider them to be in a state of biaxial stress, where the vertical stress σ_v is caused by the bond in the steel-concrete interface and the hoop stress σ_h is induced by the lateral expansion of the UHPC. In order to calculate these stresses from the strain gauge readings, the elastic-plastic analysis method presented in [25] and also used in [47] was employed. The method is based in the 'deformation theories' of

plasticity and allows the stress components (σ_v, σ_h) in the stainless steel tube in the elastic and plastic stages to be calculated as follows:

Elastic stage (Hooke's law)
$$\begin{bmatrix}\sigma_h\\ \sigma_v\end{bmatrix} = \frac{E_0}{1-\mu_s^2}\begin{bmatrix}1 & \mu_s\\ \mu_s & 1\end{bmatrix}\begin{bmatrix}\varepsilon_h\\ \varepsilon_v\end{bmatrix} \quad (1)$$

Plastic stage
$$\begin{bmatrix}\sigma_h\\ \sigma_v\end{bmatrix} = \frac{E_s^t}{1-\mu_{sp}^2}\begin{bmatrix}1 & \mu_{sp}\\ \mu_{sp} & 1\end{bmatrix}\begin{bmatrix}\varepsilon_h\\ \varepsilon_v\end{bmatrix} \quad (2)$$

where μ_{se} and μ_{sp} represent the Poisson's ratio of stainless steel in the elastic and plastic stages, respectively. E_0 and E_{st} refer to the elastic modulus and the secant modulus in the plastic stage. The full equations for μ_{sp} and E_{st} are detailed in [25]. Once σ_v and σ_h are determined, the equivalent (von Mises) stress σ_z is calculated from Eq. (3):

$$\sigma_z = \sqrt{\sigma_h^2 + \sigma_v^2 - \sigma_h\sigma_v} \quad (3)$$

Fig. 12 presents the calculated stress development in the stainless steel tube at mid-height for all monotonically loaded specimens. The point of first yield (i.e. $\sigma_z = f_y$) is also indicated on the load-stress curves. It is seen that yielding is typically initiated before the specimen reaches the peak load, on average at about 93% of the capacity. This implies that the steel tube has already entered the strain-hardening range when the peak load is attained in the SS+UHPC columns. This also stands in contrast with test results on conventional carbon steel tube confined concrete (STCC) columns, where it was observed that the steel tube yields in the very near vicinity of the peak load or even in the post-peak stage [17, 18].

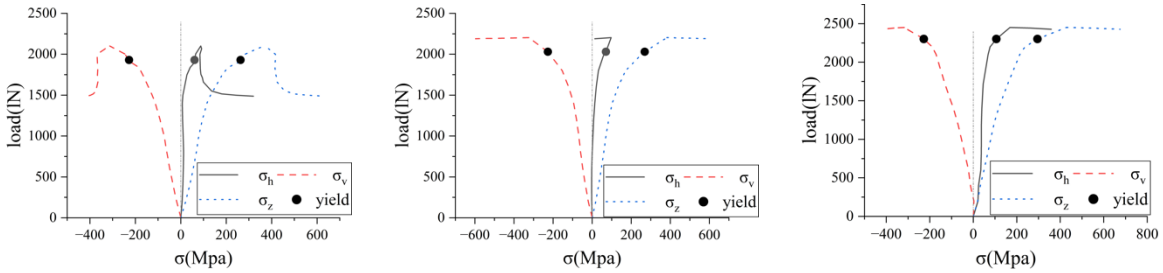

(a) T133-3-a (b) T133-4-a (c) T133-6-a

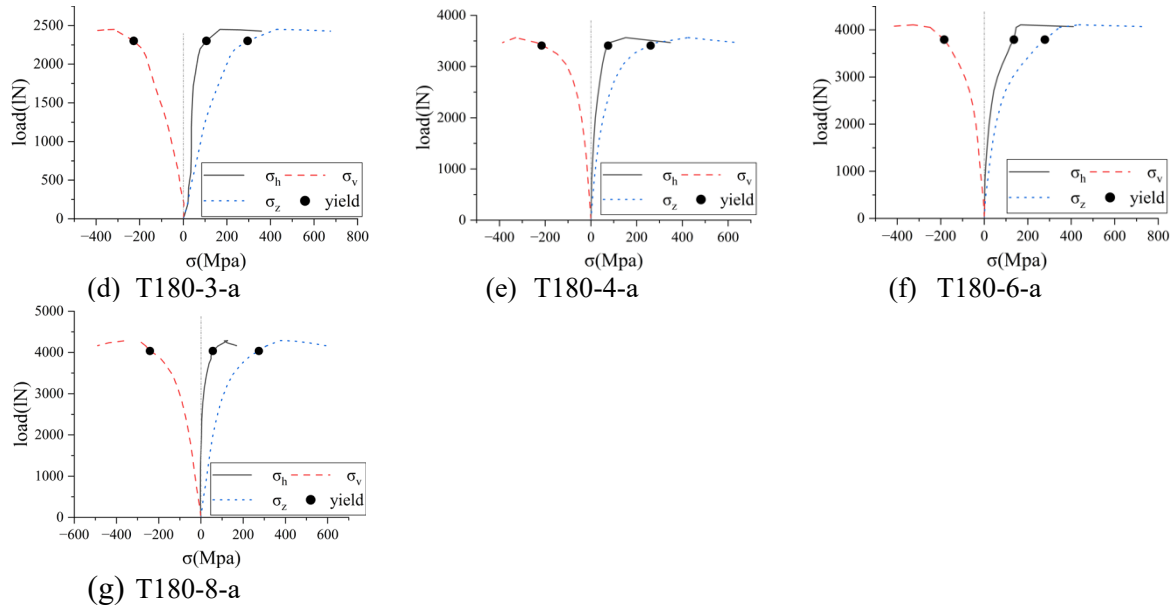

Fig. 12 Load-stress curves of monotonically loaded specimens

3.4 Axial capacity, ductility and stiffness degradation

The axial capacity N_u of the SS+UHPC columns was taken as the peak load in the load-displacement curves shown in Fig. 10. A comparison of N_u across all tested specimens is provided in Fig.13 (a) & (b). It is seen, rather unsurprisingly, that an increase in the tube thickness for an otherwise constant geometry results in an improvement in the axial capacity regardless of the loading scheme, but also that the cyclically loaded specimens consistently exhibited a slightly lower capacity than their monotonically loaded counterparts. The reduction ranges from 2.14% to 7.81%, with Fig.13 (b) suggesting that a higher *D/t* ratio generally brings about a slightly larger reduction, or equivalently that a thicker stainless steel tube is slightly less prone to deterioration under cyclic loading.

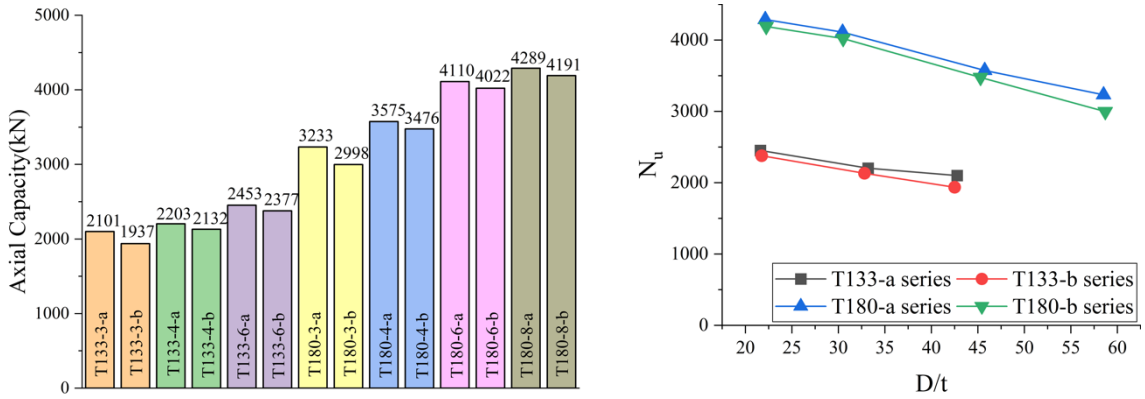

(a) Axial capacity (N_u)

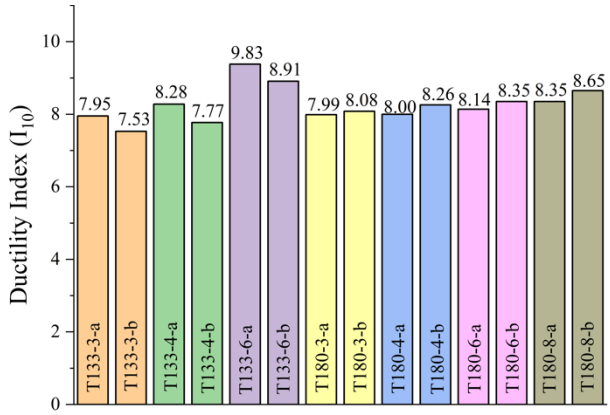

(b) Effect of D/t on N_u

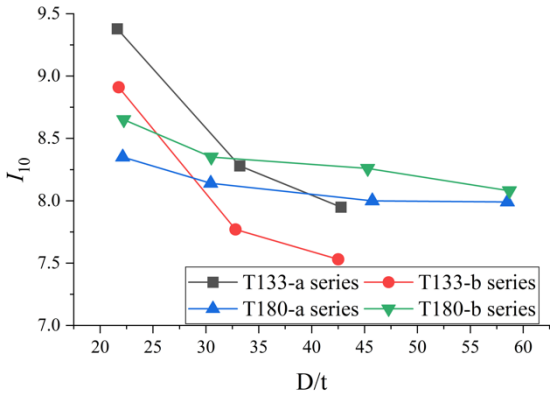

(c) Ductility index (I_{10})

(d) Effect of D/t on I_{10}

Fig. 13 Axial capacity and ductility of SS+UHPC columns

The ductility performance of the SS+UHPC columns was quantified using the I_{10} index, which is a commonly employed energy-based ductility index for ductile members, as opposed to the displacement-based ductility indices [48]. I_{10} is calculated as the ratio of the area enclosing the load vs. axial strain curve up to 5.5 times the yield strain to the area corresponding to the yield strain [21]. For the cyclically loaded specimens, the skeleton curve was used. The results are compared in Fig. 13 (a). It is concluded that I_{10} exceeds 7.0 for all specimens, and increases with increasing tube thickness for both the monotonically and cyclically loaded specimens. In the post-peak stage, the damage accumulation in the UHPC impairs the ductility; however, the work hardening effect in the stainless steel leads to increasing confining pressures which prove beneficial. Fig. 13 (b) shows that the ductility is negatively affected by the D/t ratio, with the T133 series being more sensitive to this parameter than the T180 series. This could potentially indicate a size effect, or may be linked to the fact that the measured yield stress f_y decreases between the T133 specimens with D/t = 22 and D/t = 33, while f_y increases for the equivalent T180 specimens (see Table 1). The difference in ductility between the monotonic and cyclic loading schemes was small and varied from 1.13% to 6.15%.

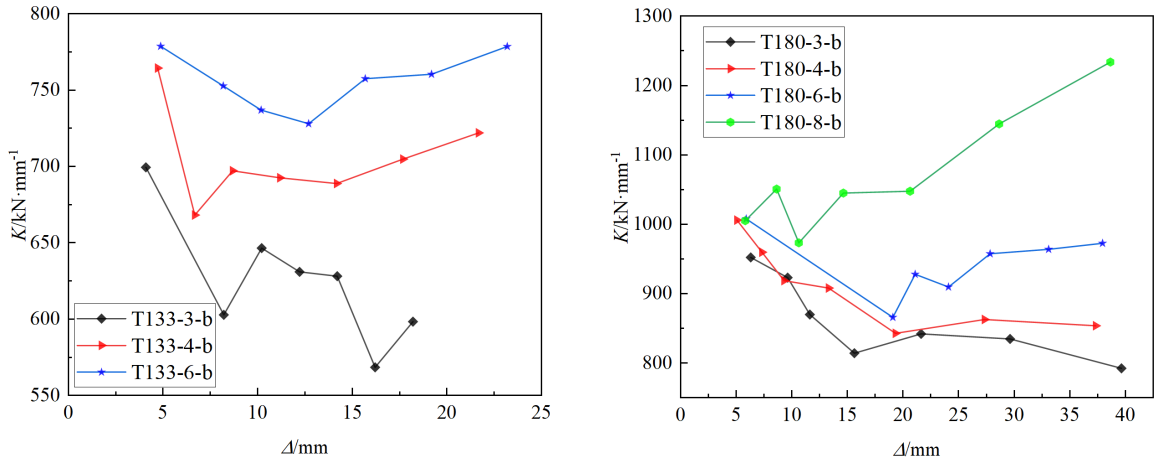

(a) T133 series (b) T180 series

Fig. 14 Axial stiffness degradation of cyclically loaded SS+UHPC columns

Fig. 14 displays the stiffness degradation of the cyclically loaded specimens, where the abscissa of each data point represents the axial displacement at the onset of an unloading cycle, and the ordinate represents the axial stiffness K, which is defined as the secant stiffness calculated from the start and end points of each unloading cycle. It is concluded that smaller D/t ratios result in a higher stiffness and a slower reduction rate over the course of loading, reflecting that for a given cross-sectional diameter the steel tube thickness has a positive effect on confinement. In addition, it is observed that the stiffness of all SS+UHPC columns remains at a relatively high level despite significant axial deformation. For the specimens with a D/t ratio below 32, the stiffness even experiences a recovery trend, attributed to the work hardening effect in the stainless steel tube.

4. Design model

4.1 Assessment of the confinement effect

As previously explained and illustrated in Fig.15 (a), the stainless steel tube in the SS+UHPC columns is subjected to a biaxial stress state, while the infilled UHPC is in triaxial compression. The strength index (SI) is a widely used indicator to quantify the confinement effect in STCC columns. The SI is defined as the ratio of the measured axial capacity to the calculated capacity based on simple superposition:

$$SI = \frac{N_{u,t}}{A_s f_y + A_c f_{co}} \tag{4}$$

where A_s and A_c refer to the cross-sectional area of the stainless steel tube and the UHPC core, respectively.

Fig. 15 (b) plots the SI as a function of the confinement factor ξ, defined as:

$$\xi = \frac{A_s f_y}{A_c f_{co}} \tag{5}$$

It is seen that all specimens have an SI value exceeding 1.0, and a few specimens even surpass 1.30, indicating significant strength gains from the confinement effect. It is also observed that the SI is positively affected by ξ, which is consistent with previous studies on STCC columns [32]. The T133 series appears less sensitive to ξ, which may possibly be caused by a size effect or may simply be a result of the limited number of specimens tested. This warrants further investigation.

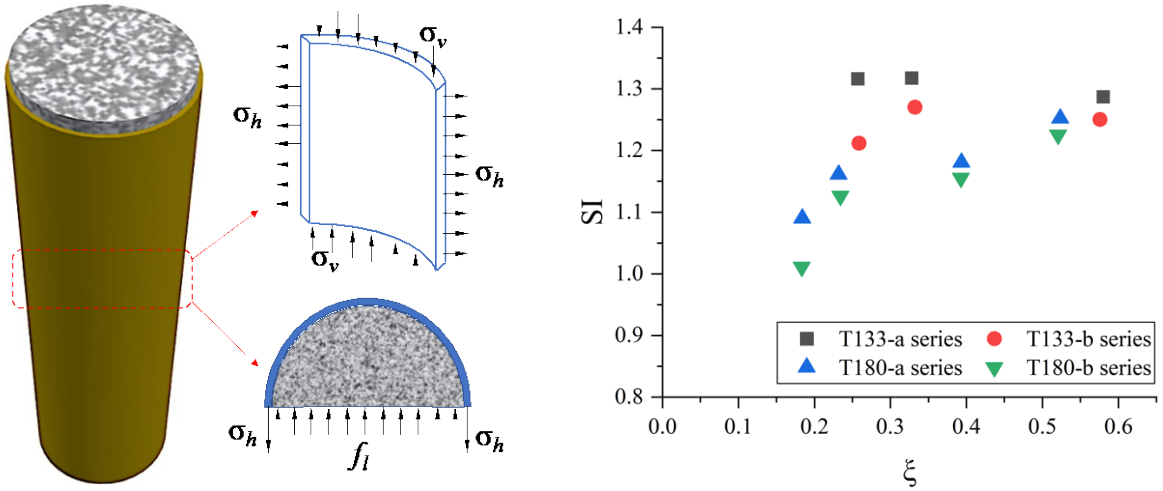

(a) Confinement mechanism (b) Strength index

Fig. 15 Assessment of confinement effect in SS+UHPC columns

4.2 Analysis of the confinement effect

As illustrated in Fig. 15 (a), the confining pressure f_l acting on the UHPC core can be calculated from the hoop stress σ_h based on force equilibrium:

$$f_l = \frac{2t}{D-2t}\sigma_h \quad (6)$$

On the other hand, the axial force resisted by the SS+UHPC columns is obtained by superimposing the load carried by the stainless steel tube and the UHPC core:

$$N_u = A_s\sigma_v + A_c f_{cc} \quad (7)$$

In Eqs. (6) and (7) σ_h and σ_v can be obtained from the strain gauge measurements using Eqs. (1-2). Eq. (6) then yields the confining pressure f_l, while Eq. (7), with the use of the measured capacity N_u, reveals the confined UHPC compressive strength f_{cc}. The stress ratios σ_v/f_y and σ_h/f_y of the seven monotonically loaded specimens at their peak load are plotted in Fig. 16. The axial stress σ_v at the peak load varied from 1.0 f_y to 1.24 f_y, while the corresponding hoop stress σ_h varied from 0.32 f_y to 0.58 f_y. This results in an equivalent stress σ_z exceeding the yield strength of the tube material, demonstrating that the stainless steel is in its strain-hardening stage at the column's peak load.

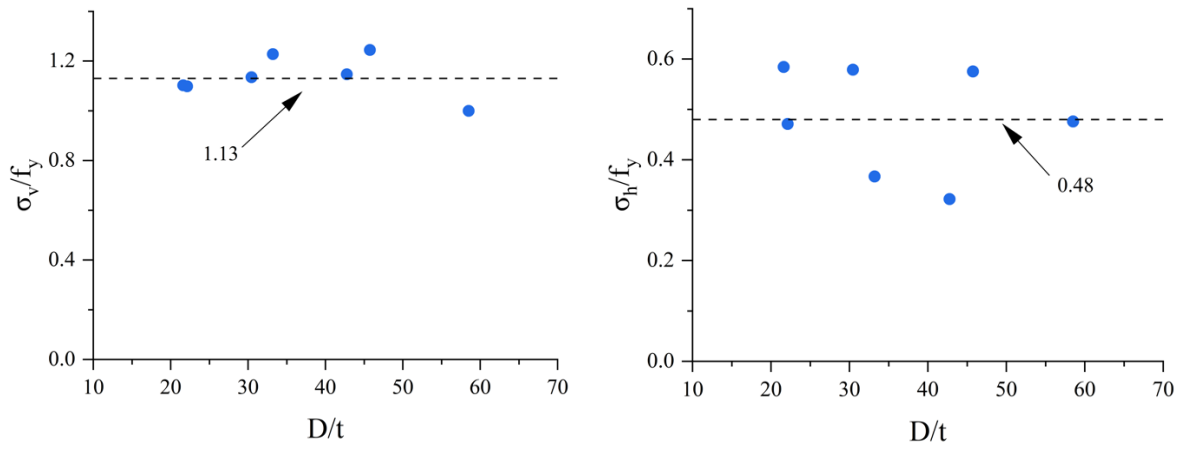

(a) Longitudinal stress (b) Transverse stress

Fig. 16 Calculated stresses at peak load: (a) σ_v/f_y versus D/t and (b) σ_h/f_y versus D/t.

The values of the confined compressive strength f_{cc} of the UHPC are summarized in Table 2. The confined strength ratio f_{cc}/f_{co} varied from 1.11 to 1.39 with an average value of 1.27. These values are higher than those typically encountered in comparable CFST columns [35]. For comparative purposes, a few alternative equations to calculate f_{cc} available in the literature are summarized in Table 3, with their numerical predictions also listed in Table 2. All of these

models calculate f_{cc} as a function of the unconfined strength f_{co} and the confining pressure f_l. Eq. (6) was used to calculate f_l from the test results. It is noted that Eq. (8), proposed by Mander et al. [49], and Eq. (11), proposed by Richart et al. [52], were originally derived for reinforced concrete columns, but they are also commonly employed for STCC columns. Table 2 reveals that all four alternative models overestimate the confined compressive strength of the UHPC, although the margin of error reduces in the order they are listed (i.e. Eq. (8) to Eq. (11)). The classical Mander model even overestimates f_{cc} by 17%, implying that these confinement models are not applicable to predict the axial capacity of SS+UHPC columns.

Table 2 Predictions of confined concrete strength

Specimen	ξ	SI	$f_{cc,t}$ (MPa)	f_{cc}/f_{co}	Mander		Xiao		Li		Richart	
					$f_{cc,p}$ (MPa)	$f_{cc,p}/f_{cc,t}$	$f_{cc,p}$ (MPa)	$f_{cc,p}/f_{cc,t}$	$f_{cc,p}$ (MPa)	$f_{cc,p}/f_{cc,t}$	$f_{cc,p}$ (MPa)	$f_{cc,p}/f_{cc,t}$
T133-3-a	0.26	1.32	145.04	1.36	133.90	0.92	133.16	0.92	129.45	0.89	124.31	0.86
T133-4-a	0.33	1.32	143.66	1.35	144.59	1.01	142.23	0.99	137.96	0.96	132.15	0.92
T133-6-a	0.58	1.29	148.71	1.39	194.84	1.31	186.88	1.26	175.41	1.18	177.12	1.19
T180-3-a	0.18	1.09	118.02	1.11	135.55	1.15	134.56	1.14	130.77	1.11	125.48	1.06
T180-4-a	0.23	1.16	121.77	1.14	148.51	1.22	145.55	1.20	141.02	1.16	135.17	1.11
T180-6-a	0.39	1.18	127.81	1.20	171.85	1.34	165.78	1.30	158.75	1.24	154.77	1.21
T180-8-a	0.52	1.25	142.12	1.33	175.40	1.23	168.95	1.19	161.38	1.14	158.02	1.11
					Ave	1.17		1.14		1.10		1.07
					St.d	0.155		0.139		0.125		0.133

Table 3 Equations for the calculation of f_{cc}

Source	Equations	
Mander et al. [49]	$f_{cc} = f_{co}\left(-1.254 + 2.254\sqrt{1 + 7.94\frac{f_l}{f_{co}}} - 2\frac{f_l}{f_{co}}\right)$	(8)
Xiao et al. [50]	$f_{cc} = f_{co}\left(1 + 3.24\left(\frac{f_l}{f_{co}}\right)^{0.8}\right)$	(9)
Li & Du [51]	$f_{cc} = f_{co}\left(-0.413 + 1.413\sqrt{1 + 11.4\frac{f_l}{f_{co}}} - 2\frac{f_l}{f_{co}}\right)$	(10)
Richart et al. [52]	$f_{cc} = f_{co} + 4.1f_l$	(11)

4.3 Proposed design equations

Eq. (7) indicates that the longitudinal stress in the stainless steel tube, σ_v, and the confined UHPC compressive strength, f_{cc}, are needed to predict the axial capacity of SS+UHPC columns. Based on Fig. 16 (a), σ_v was conservatively taken as 1.1 f_y. A new equation was derived to calculate f_{cc} of the UHPC based on the confining pressure f_l, given the conclusions obtained from Table 2 and the inadequacy of current equations. Fig. 17 (a) presents the variation of f_{cc}/f_{co} with respect to different confining pressures f_l. Based on a linear regression analysis, Eq. (12) was proposed. As a simplifying assumption, σ_h was taken to be 0.48 f_y according to the average value shown in Fig. 16 (b):

$$f_{cc} = f_{co}\left[1 + 3\frac{2t}{(D-2t)}0.48\frac{f_y}{f_{co}}\right] \tag{12}$$

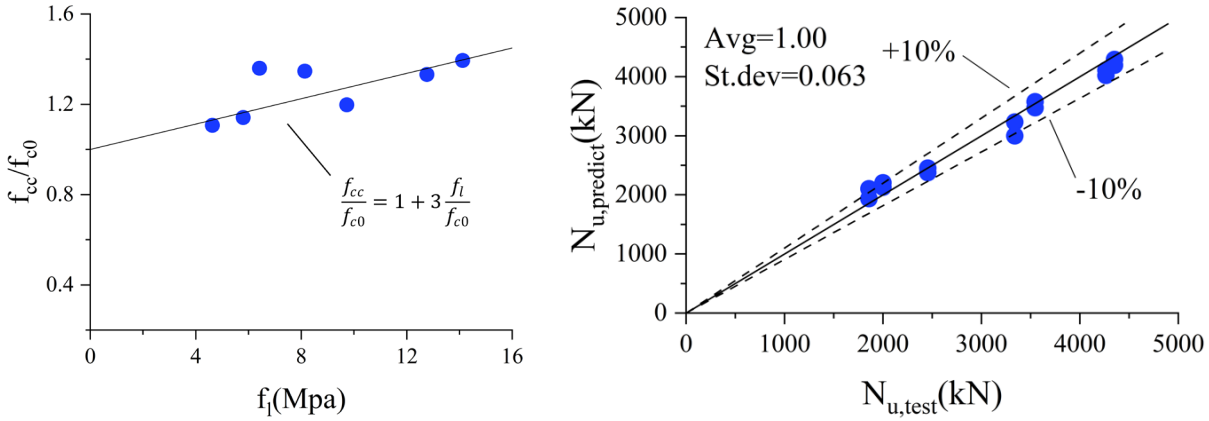

(a) Relation between f_{cc}/f_{co} and f_l (b) Comparison between predicted and test result

Fig. 17 Evaluation of the proposed formula

The axial capacity of SS+UHPC columns can then be calculated as:

$$N_u = 1.1A_s f_y + \left[1 + \frac{2.88f_y}{(D/t-2)f_{co}}\right]A_c f_{co} \tag{13}$$

Although Eq. (13) has been derived for monotonically loaded specimens, it can also be employed to evaluate the capacity of cyclically loaded specimens, as the loading scheme was found to have a minor effect on the axial capacity. Fig. 17 (b) shows that excellent agreement is achieved between the predicted and tested axial capacities, with an average ratio of 1.00. Moreover, all data points fall within the ±10% error lines, with the standard deviation

amounting to 0.063, demonstrating that the proposed formulae can reliably be used to determine the axial capacity of SS+UHPC columns.

5. Conclusions and recommendations

This paper proposes a novel type of composite column (SS+UHPC), characterized by excellent durability, axial capacity and ductility. An experimental program was conducted to investigate the axial performance of SS+UHPC columns subjected to either monotonic or cyclic axial compressive loading. Based on experimental observations of the actual stress state in the stainless steel tube and the UHPC core, a design formula was proposed to predict the axial load capacity of SS+UHPC columns. The research led to the following conclusions:

1. Owing to the inherent brittleness of the UHPC, all SS+UHPC column specimens experienced an abrupt drop in load upon reaching the peak load. Specimens with a *D/t* ratio less than 22 in this programme generally failed in a bulging mode, with a less severe drop in load and with the load-displacement curves exhibiting a hardening trend at the post-peak stage. Specimens with *D/t* ratios exceeding 22 failed in a diagonal shear mode, with the residual capacity stabilizing at 72% - 81% of the peak load. This was the case for both monotonic and cyclic loading.
2. The stainless steel tube was subjected to a biaxial stress state due to the combined effects of friction in the interface between the materials (causing longitudinal compression) and the hoop stresses induced by the lateral expansion of the UHPC. At the peak load, the longitudinal stress in the stainless steel tube σ_v reached 1.0 f_y to 1.24 f_y, while the hoop stress σ_h reached 0.32 f_y to 0.58 f_y. The latter resulted in an average confined strength ratio f_{cc}/f_{co} of 1.27 in the UHPC, indicating a strong confinement effect.

3. The confinement effect in the UHPC was activated before the peak load. The equivalent (von Mises) stress σ_z reached the yield strength at around 93% of the peak load in the ascending load stage.
4. The cyclically loaded specimens exhibited a slightly lower capacity than their monotonic counterparts. The reduction ranged from 2.14% to 7.81%, and diminished with lower *D/t* ratios. Regardless of the loading scheme, lower *D/t* ratios also resulted in improvements in axial capacity and ductility index. Some cyclically loaded specimens exhibited enhanced ductility over their monotonic counterparts due to work hardening, although the difference remained limited to 6.15%. In the cyclically loaded specimens, decreasing the *D/t* ratio had a beneficial effect on the stiffness degradation.
5. Previously developed empirical formulae overestimated the confinement effect in the SS+UHPC columns by 7% to 17%. A new equation is proposed to predict the axial capacity of SS+UHPC columns, which delivers good accuracy (average ratio of predicted to experimental capacity of 1.0) with a small standard deviation of 6.3%.

Data availability

The database will be made available on request.

Acknowledgement

This study was jointly supported by the Open Project of Key Lab of Structures Dynamic Behavior and Control of the Ministry of Education, Harbin Institute of Technology, under grant number of 2022HITCE05, and the Fundamental Research Funds for the Central Universities under grant number of 2242022k30030 and 2242022k30031.

References

[1] Zhao J, Lai BL, Fan S, et al. Numerical simulation of local-distortional buckling behavior of lipped C-section stainless steel columns. Journal of Constructional Steel Research, 2023, 211: 108148.

[2] Chen MH, Fan SG, Tao YL, Li S, Liu MJ. Design of the distortional buckling capacity of stainless steel lipped C-section columns, Journal of Constructional Steel Research, 2018, 147: 116–131.

[3] Zhou F, Lama L, Zhao K. Design of stainless steel CHS-concrete infill-carbon steel CHS double-skin stub columns. Engineering Structures, 2023, 278: 115479.

[4] Lai BL, Zheng XF, Fan SG, et al. Behavior and design of concrete filled stainless steel tubular columns under concentric and eccentric compressive loading. Journal of Constructional Steel Research, 2024, 213: 108319.

[5] Zhao Z, Wei Y, Wang G, et al. Axial compression performance of circular UHPC-filled stainless-steel tubular columns. Engineering Structures, 2024, 302: 117430.

[6] Tang H, Wang H, Liu Y, et al. Axial compressive property of square and rectangular UHPC-filled duplex stainless steel tube stub columns. Composite Structures, 2023, 323: 117492.

[7] Zhao Z, Wei Y, Yue P, et al. Axial compression and load-carrying performance of rectangular UHPC-filled stainless-steel tubular short columns. Journal of Constructional Steel Research, 2024, 213: 108397.

[8] Zhao Z, Wei Y, Wang G, et al. Axial compression performance of square UHPC-filled stainless-steel tubular columns. Construction and Building Materials, 2023, 408: 133622.

[9] Dai P, Yang L, Wang J, et al. Compressive strength of concrete-filled stainless steel tube stub columns. Engineering Structures, 2020, 205: 110106.

[10] Ma K, Zhou Q, Li L, et al. Experimental study on concrete-filled stainless steel tubular stub columns under axial compression load.Structures, 2024, 63: 106436.

[11] Han LH, Xu CY, Hou C. Axial compression and bond behaviour of recycled aggregate concrete-filled stainless steel tubular stub columns. Engineering Structures, 2022, 262: 114306.

[12] Lai BL, Li YR, Jin L, Fan SG. Experimental study on the compressive behavior of UHPC filled stainless steel tubes subjected to monotonic and cyclic loading. Construction and Building Materials, 2024, 449: 138301.

[13] Ellobody E, Ghazy MF. Experimental investigation of eccentrically loaded fibre reinforced concrete-filled stainless steel tubular columns. Journal of Constructional Steel Research, 2012, 76: 167–176.

[14] Lam D, Gardner L. Structural design of stainless steel concrete filled columns. Journal of Constructional Steel Research, 2008, 64(11): 1275–1282.

[15] Dabaon MA, El-Boghdadi MH, Hassanein MF. Experimental investigation on concrete-filled stainless steel stiffened tubular stub columns. Engineering Structures, 2009, 31(2): 300–307.

[16] Uy B, Tao Z, Han LH. Behaviour of short and slender concrete-filled stainless steel tubular columns. Journal of Constructional Steel Research, 2011, 67(3): 360–378.

[17] Liu J, Zhou X, Gan D. Effect of friction on axially loaded stub circular tubed columns. Advances in Structural Engineering, 2016, 19(3): 546-559.

[18] Liu J, Zhou X. Behavior and strength of tubed RC stub columns under axial compression. Journal of Constructional Steel Research, 2010, 66(1): 28-36.

[19] Qi H, Guo L, Liu J, et al. Axial load behavior and strength of tubed steel reinforced-concrete (SRC) stub columns. Thin-Walled Structures, 2011, 49(9): 1141-1150.

[20] Lai BL, Liew JYR, Xiong M. Experimental study on high strength concrete encased steel composite short columns. Construction and Building Materials, 2019, 228: 116640.

[21] Lai, BL, Liew, JYR, Le Hoang A. Behaviour of high strength concrete encased steel composite stub columns with C130 concrete and S690 steel. Engineering Structures 2019; 200:109743.

[22] Lai B, Liew JYR. Design and testing of concrete encased steel composite beam-columns with C90 concrete and S690 steel section. Engineering Structures 2020;220:110995.

[23] Lai B, Liew JYR. Axial-moment interaction of high strength concrete encased steel composite columns: Experimental investigation. Journal of Constructional Steel Research, 2020, 175: 106370.

[24] O'Shea M D, Bridge RQ. Design of circular thin-walled concrete filled steel tubes. Journal of Structural Engineering, 2000, 126 (11): 1295-1303.

[25] Guo L, Liu Y, Fu F, et al. Behavior of axially loaded circular stainless steel tube confined concrete stub columns. Thin-Walled Structures, 2019, 139: 66-76.

[26] Li W, Zha X, Wang H. A unified formulation for axial compression of steel tube-confined concrete and concrete-filled steel tube stub columns. Structures, 2023, 58: 105319.

[27] Zhang S, Liu J. Seismic behavior and strength of square tube confined reinforced-concrete (STRC) columns. Journal of Constructional Steel Research, 2007, 63(9): 1194-1207.

[28] Liu J, Zhang S, Zhang X, et al. Behavior and strength of circular tube confined reinforced-concrete (CTRC) columns. Journal of Constructional Steel Research, 2009, 65(7): 1447-1458.

[29] Liu J, Teng Y, Zhang Y, et al. Axial stress-strain behavior of high-strength concrete confined by circular thin-walled steel tubes. Construction and Building Materials, 2018, 177: 366-377.

[30] Le Hoang A, Fehling E. Numerical study of circular steel tube confined concrete (STCC) stub columns. Journal of Constructional Steel Research, 2017, 136: 238-255.

[31] Le Hoang A, Fehling E, Lai BL, et al. Experimental study on structural performance of UHPC and UHPFRC columns confined with steel tube. Engineering Structures, 2019, 187: 457-477.

[32] Qiao QY, Yang ZY, Cao WL. Axial compressive behavior of stainless steel tube confined concrete column piers. Marine Structures, 2021, 78: 103021.

[33] Lai BL, Liew JYR, Venkateshwaran A, et al. Assessment of high-strength concrete encased steel composite columns subject to axial compression. Journal of Constructional Steel Research, 2020, 164: 105765.

[34] Liew JYR, Xiong MX, Lai BL. Design of Steel-Concrete Composite Structures Using High-Strength Materials. Woodhead Publishing, 2021.

[35] Xiong MX, Xiong DX, Liew JYR. Axial performance of short concrete filled steel tubes with high-and ultra-high-strength materials. Engineering Structures, 2017, 136: 494-510.

[36] Lai BL, Liew JYR, Xiong MX. Experimental and analytical investigation of composite columns made of high strength steel and high strength concrete. Steel and Composite Structures, An International Journal, 2019, 33(1): 67-79.

[37] GB/T 228-2002, Metallic Materials-Tensile Testing at Ambient Temperature. Beijing, China, 2002.

[38] GB/T 50081-2002, Standard for Test Method of Mechanical Properties on Ordinary Concrete. Beijing, China, 2002.

[39] Lai BL, Zhang M Y, Chen ZP, et al. Axial compressive behavior and design of semi-precast steel reinforced concrete composite columns with permanent ECC formwork. Structures, 2023, 57: 105130.

[40] Lai BL, Zhang M Y, Zheng XF, et al. Experimental study on the axial compressive behaviour of steel reinforced concrete composite columns with stay-in-place ECC jacket. Journal of Building Engineering, 2023, 68: 106174.

[41] Haber ZB, Munoz JF, De la Varga I, et al. Bond characterization of UHPC overlays for concrete bridge decks: Laboratory and field testing. Construction and Building Materials, 2018, 190: 1056-1068.

[42] Fang Y, Wang Y, Zhang B, et al. Behaviour of concrete-filled thin-walled corrugated steel tubes under cyclic axial compression. Thin-Walled Structures, 2021, 162: 107630.

[43] Chen S, Zhang R, Jia LJ, et al. Structural behavior of UHPC filled steel tube columns under axial loading. Thin-walled structures, 2018, 130: 550-563.

[44] American Society for Testing and Materials (ASTM), Standard Test Methods for Cyclic (Reversed) Load Test for Shear Resistance of Framed Walls for Buildings. ASTM E2126, West Conshohocken, USA, 2007.

[45] Milad M, Zreiba N, Elhalouani F, et al. The effect of cold work on structure and properties of AISI 304 stainless steel. Journal of materials processing technology, 2008, 203(1-3): 80-85.

[46] Kant C, Harmain G A U. Effect of cold working on mechanical properties of pure-304L stainless steel with variable temperature-an experimental study. Advances in Materials and Processing Technologies, 2023: 1-21.

[47] Zhang S, Guo L, Ye Z, et al. Behavior of steel tube and confined high strength concrete for concrete-filled RHS tubes. Advances in Structural Engineering, 2005, 8(2): 101-116.

[48] Lai BL, Bao RL, Zhang MY, et al. Evaluation on the static and seismic performance of steel reinforced concrete composite columns with high strength materials. Journal of Building Engineering, 2023, 79: 107886.

[49] Mander J B, Priestley M J N, Park R. Theoretical stress-strain model for confined concrete. Journal of structural engineering, 1988, 114(8): 1804-1826.

[50] Xiao QG, Teng JG, Yu T. Behavior and modeling of confined high-strength concrete. Journal of Composites for Construction, 2010, 14(3): 249-259.

[51] Li Z, Du GF. Finite element analysis of mechanical properties and bearing capacity calculation for square steel tube confined concrete short columns under axial compression. Journal of Building Structures, 2016;37(2016S1):245–50.

[52] Richart F E, Brandtzæg A, Brown R L. A study of the failure of concrete under combined compressive stresses. University of Illinois. Engineering Experiment Station. Bulletin; no. 185, 1928.